Geochemistry Geophysics Geosystems G3

Article
Volume 11, Number 12
15 December 2010
Q12006, doi:10.1029/2010GC003301
ISSN: 1525-2027

Published by AGU and the Geochemical Society

Global slab deformation and centroid moment tensor constraints on viscosity

L. A. Alpert, T. W. Becker, and I. W. Bailey
Department of Earth Sciences, University of Southern California, 3651 Trousdale Parkway, Los Angeles, California 90089-0740, USA (laalpert@usc.edu)

[1] We analyze moment tensor solutions from deep subduction zone earthquakes to determine global slab deformation patterns. Inferred strain rates are compared to predicted deformation patterns from fluid models to help constrain the first-order radial and lateral viscosity structure of the Earth. While all slabs that reach the lower mantle are compressed at their tip, intermediate depth patterns are more complex. We compute 3-D spherical flow with various slab rheologies and compare the angular misfit between the compressive eigenvectors of the resultant stress field and global centroid moment tensor (gCMT) solutions. We find that upper mantle slab viscosities of ~10–100 and lower mantle viscosities of ~30–100 times the upper mantle produce the best match to gCMTs. A 0.1 viscosity reduction in the asthenosphere seems preferred. Slab geometry and lower mantle viscosity exert significant control on deformation. Inclusion of the phase changes at 410 km and 660 km increases extensional deformation at intermediate depth and compressional deformation at the lower mantle, improving the match to gCMTs for strong slabs. Our conclusions are fairly insensitive to surface boundary conditions. However, models which include net rotations of the surface with respect to the lower mantle produce compression at intermediate depths for west directed slabs and extension for east directed slabs. Without allowing for regional variations, these models yield the best match to gCMTs. While significant deviations between model and seismicity remain, our results show that seismicity provides an underutilized constraint for slab dynamics.

Components: 12,200 words, 17 figures, 4 tables.

Keywords: subduction; mantle rheology; slab deformation; plate motions; net rotation; phase transitions.

Index Terms: 8162 Tectonophysics: Rheology: mantle (8033); 7240 Seismology: Subduction zones (1207, 1219, 1240); 0545 Computational Geophysics: Modeling (1952, 4255).

Received 16 July 2010; **Revised** 1 October 2010; **Accepted** 15 October 2010; **Published** 15 December 2010.

Alpert, L. A., T. W. Becker, and I. W. Bailey (2010), Global slab deformation and centroid moment tensor constraints on viscosity, *Geochem. Geophys. Geosyst.*, *11*, Q12006, doi:10.1029/2010GC003301.

1. Introduction

[2] Subducting lithospheric slabs coupled to surface plates exert a pull force that contributes to plate motions [e.g., *Forsyth and Uyeda*, 1975]. In the upper mantle, flow induced by slab density exerts tractions on the base of plates that further contribute to surface motions. Together, these forces act to make subducting slabs the main driving force for plate tectonics [e.g., *Lithgow-Bertelloni and Richards*, 1998; *Becker and O'Connell*, 2001; *Conrad and Lithgow-Bertelloni*, 2002]. Geodynamic models with only radial viscosity variations and dense slabs are sufficient for reproducing relative plate motions [e.g., *Ricard and Vigny*, 1989]. However, lateral viscosity variations (LVVs) are required to speed up oceanic compared to continental plates [*Conrad and Lithgow-Bertelloni*, 2002; *Becker*, 2006] and

Copyright 2010 by the American Geophysical Union

to induce the net rotation of the lithosphere as observed in plate motion models [e.g., *Ricard et al.*, 1991]. The strength of slabs relative to the mantle, which may constitute an important component of LVVs, is, however, still a matter of debate (see reviews by *Billen* [2008] and *Becker and Faccenna* [2009], for example), as are variations in viscosity with depth in the mantle [e.g., *Mitrovica and Forte*, 2004].

[3] Geodynamic models often invoke a layer of reduced viscosity beneath the lithosphere as well as an increase in viscosity in the lower mantle. The existence of a low-viscosity layer between the lithosphere and the transition zone at ~300 km is supported by rock rheology [e.g., *Hirth and Kohlstedt*, 2004] and geoid studies [e.g., *Hager and Clayton*, 1989; *Mitrovica and Forte*, 2004]. Geoid studies also support an increase in viscosity with depth to support subducting slabs [*Hager*, 1984]. Models with a ~50× increase in viscosity applied to the lower mantle improve the match to the observed geoid [e.g., *Hager and Clayton*, 1989; *Forte*, 2007].

[4] Buoyancy forces from density anomalies in the upper mantle produce deformation within subducting slabs accommodated by seismic strain release [e.g., *Vassiliou and Hager*, 1988]. Strain rates calculated from seismic moments [e.g., *Bevis*, 1988] suggest that plates deform anelastically at intermediate depths. Slab geometry from seismicity and seismic tomography [e.g., *Hager and O'Connell*, 1979; *van der Hilst et al.*, 1997] images highly contorted slab shapes inconsistent with rigid, elastic plates. Such studies justify a fluid treatment of subducting slabs in numerical models. Moreover, slabs are imaged by tomography as deflected by or penetrating through the 660 km discontinuity [e.g., *van der Hilst et al.*, 1997; *Fukao et al.*, 2001]. Lower mantle slabs may also contribute to plate driving forces, though the mode of force transmission is debated [e.g., *Deparis et al.*, 1995; *Lithgow-Bertelloni and Richards*, 1995; *Becker and O'Connell*, 2001; *Stadler et al.*, 2010].

[5] Given the uncertainties about slab strength and force transmission, additional constraints from seismicity are helpful. Coseismic strain release from deep earthquakes can be imaged by focal mechanism and moment tensor solutions, from P wave first motion studies [e.g., *Isacks and Molnar*, 1969] and waveform modeling [e.g., *Dziewoński et al.*, 1981], respectively. The principal axes orientations of these solutions can be interpreted as reflecting the slab deformation state [e.g., *Isacks and Molnar*, 1969; *Giardini and Woodhouse*, 1984; *Chen et al.*, 2004]. In the classic analysis of 204 focal mechanisms by *Isacks and Molnar* [1971], stress orientations suggest slabs deform by extension as they enter the low-strength upper mantle. As the slabs become supported by the higher-strength lower mantle, they become compressed. This transition is reflected in gaps in seismicity. If seismicity is continuous, compression was observed at all depths, with the inference that the slab is fully supported by the lower mantle [*Isacks and Molnar*, 1971]. Knowledge of the slab deformation state can guide numerical modeling in an effort to constrain the rheology of the slab and mantle that produces the best match to observations. *Vassiliou and Hager* [1988] compared stress orientations from 2-D fluid models to focal mechanisms, moment tensor inversions, and summed seismicity with depth. Their results suggest that slab and lower mantle viscosities are comparable and are approximately 1 order of magnitude more viscous than the upper mantle. Similar slab viscosities were inferred by *Billen and Gurnis* [2003] and *Billen et al.* [2003] when comparing stress orientations, the geoid, strain rate, and dynamic topography to three-dimensional (3-D) regional models. Two-dimensional work by *Carminati and Petricca* [2010] explored stress orientations resulting from viscoelastic models to investigate the role of large-scale plate motions on intermediate depth deformation.

[6] In this study, we use the gCMT catalog (Global CMT Project, 2006, available at http://www.globalcmt.org/, accessed May 2008) (formerly Harvard CMT) to build a global snapshot of the deformation state of subducting slabs. Building on the work by *Vassiliou and Hager* [1988], we investigate the rheology of the slab, asthenosphere, and lower mantle in a 3-D spherical mantle flow model, considering the effects of phase transitions, lower mantle density, boundary conditions, and net rotation of the lithosphere with respect to the lower mantle. We compare stresses produced by the flow model to the gCMTs by calculating the 3-D angular misfit between compressional (P) axes orientations in regions of deeply extending seismicity. Our goal is to constrain the first-order radial and lateral viscosity structure of the Earth that is complementary to the existing results from geoid, dynamic topography and plate motion studies.

[7] We find that upper mantle slab viscosities of ~10–100, lower mantle viscosities of ~30–100, and asthenosphere viscosities of ~0.1 times the upper mantle produce the best match to gCMTs.

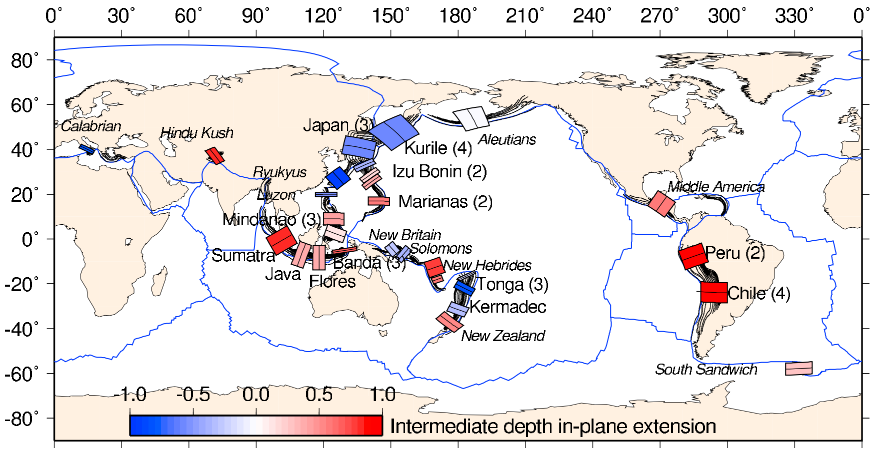

Figure 1. Twenty-four regions analyzed to obtain the slab deformation state shown in Figure 2. Boxes indicate the range of seismicity included in the cross sections. Box color is based on the average magnitude of the intermediate depth (100–350 km) extensional components of the normalized tensor summations. Of these 24 regions, 13 regions with deeply extending seismicity were used in our numerical models. For these, we divide most regions into adjacent transects, indicated by the number in parentheses beside the region name, for a total of 30 segments. Oblique names indicate regions that were not used for comparison to flow models due to the absence of deep seismicity. Blue lines indicate NUVEL-1A plate boundaries from *DeMets et al.* [1990]. For the Banda region, the box width was doubled for plotting purposes. All deeply extending slabs undergo predominantly compression at their tip, and magnitudes are shown in Figure 2. Subduction zone parameters are listed in Appendix B.

Plate kinematic forces and the net rotation generate second-order variability in intermediate depth deformation.

[8] We first present our resurvey of gCMT solutions in slabs and follow with results from numerical modeling.

2. Slab Deformation

2.1. Methods

[9] To obtain an overview of slab deformation, we generate a new global compilation of moment tensor strain orientations as a function of depth. We use the gCMT catalog with all events up to December 2008. Earthquake distribution with depth, and the depth to the transition from predominant extension to compression in subducting slabs, suggest defining ~100–350 km as intermediate and ~350–700 km as deep [e.g., *Vassiliou and Hager*, 1988] (see also Appendix A). To determine the coseismic strain orientation in subducting slabs at different depths we analyze profiles from 24 geographic regions (Figure 1). Profile parameters (Appendix B) were chosen to most closely replicate the cross sections of *Isacks and Molnar* [1971], however, some regions were divided to investigate differences along strike. We orient profiles roughly perpendicular to the strike of seismicity contours as defined by *Gudmundsson and Sambridge* [1998], then choose profile lengths and widths so that the gCMTs provide the most complete slab profile (Appendix B). For each profile, we divide the gCMT solutions into 50 km depth bins between 100 and 700 km and sum the normalized moment tensors for each bin to obtain the average coseismic strain orientation. Following *Isacks and Molnar* [1971], we exclude solutions shallower than 100 km to avoid earthquakes related to convergence.

[10] We sum normalized moment tensors [e.g., *Fischer and Jordan*, 1991; *Bailey et al.*, 2009] rather than moment tensors [*Kostrov*, 1974] due to the sensitivity of the latter to the largest earthquake considered. To obtain the slab dip corresponding to each of the depth bins we fit a polynomial to the mean hypocenter positions within the bins based on the Engdahl earthquake catalog from 1960 to 2007 [*Engdahl et al.*, 1998; E. R. Engdahl, personal communication, May 2008]. The order of the polynomial in each case is given by min(4, N_{bins-2}), where N_{bins} is the number of bins containing hypocenter data, and the fit is performed using mean depth within bins as the dependent variable and mean horizontal position within bins as the independent variable.

[11] We compute the slab dip at the mean depths within bins of the gCMTs by taking the derivative of the polynomial at that depth. We use this dip to rotate the summed tensor into a slab coordinate system, and divide the downdip component by the

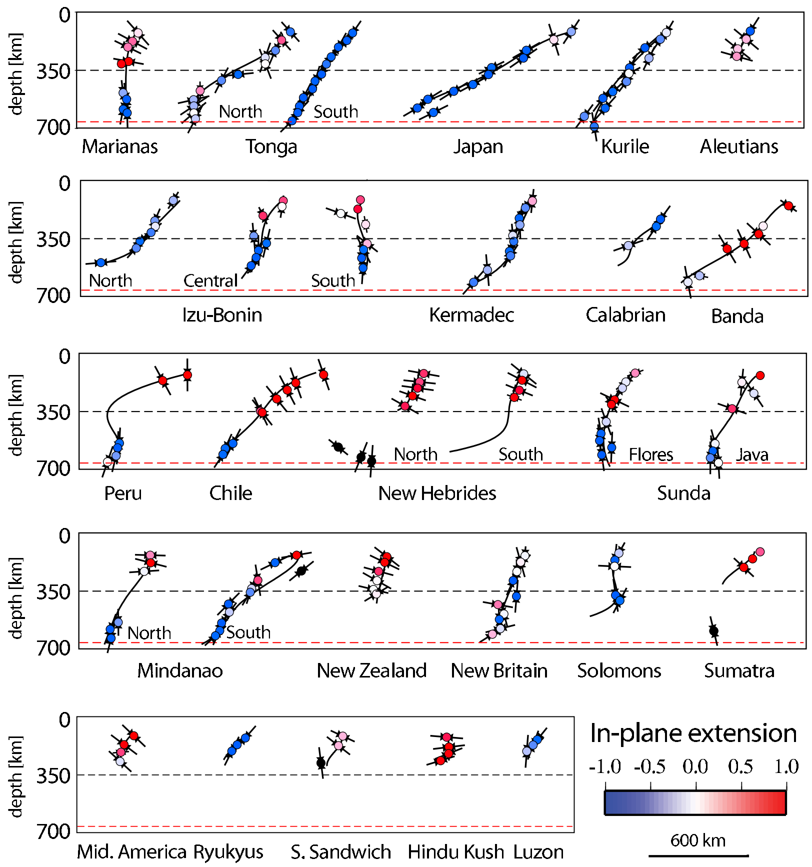

Figure 2. Results of the normalized moment tensor solutions for the subduction zones of Figure 1 (compare to *Isacks and Molnar* [1971, Figure 2]). Black lines indicate subduction zone geometry calculated by a polynomial fit to earthquake hypocenters. Circles represent summed gCMT solutions with the vectors showing the orientation of the compressional (P) axes of the solution. The circle color represents the magnitude of the extensional component of the tensor, measured parallel to the slab dip as described in section 2.1. Black filled circles represent solutions that cannot provide information on the state of stress of the slab due to inadequate constraints on the slab geometry (New Hebrides, Sumatra, and South Sandwich) or, for Mindanao, the involvement of a nearby subduction zone with reverse polarity.

eigenvalue with the largest absolute magnitude. This gives a range of −1 to 1, where −1 indicates that the dominant sense of compression is parallel to the downdip direction and 1 indicates that dominant extension is parallel. Intermediate values can result from nonalignment of the dominant axes with the slab dip, as well as from non-double-couple components that reduce the magnitude of the downdip component. These trench-parallel and slab-perpendicular forces can result from preexisting structures within the slab, complexities in slab geometry, or interaction of the slab with mantle heterogeneity.

2.2. Results

[12] As previously noted [e.g., *Carminati and Petricca*, 2010], the global slab deformation pattern can be broadly separated into predominantly intermediate extension for east directed subduction zones and predominantly intermediate compression for west directed subduction zones (Figure 1). Previous workers have recognized intermediate depth complexity and explanations invoke stresses from unbending after entering the trench [*Astiz et al.*, 1988], mechanical heterogeneities [*Isacks and Molnar*, 1971; *Chen et al.*, 2004], complex geometries [*Apperson and Frohlich*, 1987], response to deformation during convergence with the upper plate [*Isacks and Molnar*, 1971; *Bilek et al.*, 2005], interaction with lower mantle density anomalies [*Gurnis et al.*, 2000], and the net rotation of the lithosphere with respect to the lower mantle [*Carminati and Petricca*, 2010]. Assessment of those slabs in Figure 1 aligned and opposing typical net rotation directions for the present day generally supports this hypothesis, though there are some exceptions (e.g., Marianas and South Izu-Bonin).

[13] Figure 2 illustrates our inferred slab geometry and stress states with depth for the regions analyzed. While all slabs that interact with the lower mantle are predominantly under in-plane compression at their tip, intermediate depth deformation patterns are more complex [cf. *Vassiliou and Hager*, 1988].

3. Quantitative Modeling With Flow Models

3.1. Methods

3.1.1. Seismicity Analysis

[14] Our goal is to compare stress from fluid modeling to the strain orientations of gCMT solutions to produce a model with slab and mantle rheology that results in the best match to observations. We compare stress to gCMT solutions along 30 subduction zone segments from 13 of the 24 regions shown in Figure 1. We compare only regions with deeply extending seismicity and divide most regions into adjacent transects to investigate differences along strike. Although gCMTs image strain, we assume that earthquakes at a given location are an unbiased sample of the long-term stress orientation. Comparing fluid stress to seismically recorded strain release presumes no specific mechanism for deep earthquakes, but assumes that the stresses must be oriented appropriately for an earthquake to produce the resultant moment tensor. To avoid complexities potentially related to the mantle wedge region, we compare model results to gCMT solutions from 200 km to 700 km.

[15] While Figure 2 shows normalized moment tensor summation results, stress results from our flow models are extrapolated and compared to the nearest individual gCMT solution. The model fit to a gCMT solution is quantified by the angular difference between the gCMT P axis and the most compressive eigenvector from the fluid stresses, which we refer to as the misfit. To quantify the misfit for a single subduction zone (regional misfit) we compute the average of average misfits for 100 km depth bins. The global misfit is given by the average of all of the segments. This averaging at multiple scales allows us to avoid biases due to strong clustering of gCMT locations at certain depths. Although this measure neglects the orientation of intermediate and extensive axes, we find a strong correlation between eigenvector misfits and a measure based on the tensor inner product (Appendix C), so only the more intuitive eigenvector misfits are reported.

[16] A uniform distribution of axis orientations over a half sphere is given by the probability density function $\frac{1}{2\pi}\sin(\theta)d\phi d\theta$, where ϕ is longitude and θ is colatitude. Hence, for a model where stress orientations are chosen from a uniform random distribution the expected value for the misfit would be 1 radian (57.3°). The confidence bounds for nonrandomness, however, depend on the number of values compared, which is somewhat nonintuitive given the multiple averaging performed in this study. We calculate confidence levels by numerically simulating randomly oriented axes distributed among bins with the same number as in the bins of data, subsequently performing the averaging across subduction zones and global averaging in the same manner.

3.1.2. Fluid Model

[17] To model mantle circulation we use CitcomS [*Zhong et al.*, 2000], a spherical finite element code based on Citcom [*Moresi and Gurnis*, 1996], from the Computational Infrastructure for Geodynamics (geodynamics.org). CitcomS solves the equations governing mantle circulation with a variable viscosity structure. Conservation of mass (1) and momentum (2) are solved for instantaneous Stokes flow in the Boussinesq approximation:

$$\nabla \cdot \mathbf{u} = 0, \tag{1}$$

$$-\nabla p + \nabla \cdot \left[\eta\left(\nabla \mathbf{u} + \nabla^T \mathbf{u}\right)\right] - \left(Ra_T T - Ra_{pc}\Gamma\right)\mathbf{e}_r = 0, \tag{2}$$

where p is the dynamic pressure, η is the viscosity, $\mathbf{u}$ is the velocity, T is the temperature, Ra_T is the thermal Rayleigh number scaled to the radius of the Earth, Ra_{pc} is the phase change Rayleigh number, Γ is the phase change function, and $\mathbf{e}_r$ is the unit vector in the radial direction. The strength of the thermal buoyancy is controlled by Ra_T defined as:

$$Ra_T = \frac{\rho_0 g \alpha \Delta T R^3}{\kappa \eta_0}, \tag{3}$$

where ρ_0 is the reference density, g is gravitational acceleration, ΔT is the temperature difference between the surface and the asthenosphere, α is the coefficient of thermal expansion, R is the radius of the Earth, κ is the thermal diffusivity, and η_0 is the reference viscosity.

[18] All parameters are listed in Table 1. Phase change values were chosen as end members to emphasize their effect [*Vidale and Benz*, 1982; *Bina*

Table 1. Model Parameters[a]

Variable Name	Symbol	Value
Reference viscosity	η_0	10^{21} Pa s
Radius of the Earth	R	6371 km
Thermal diffusivity	κ	10^{-6} m^2 s^{-1}
Thermal Rayleigh number	Ra_T	3.4×10^8
Temperature change between surface and asthenosphere	ΔT	1300 K
Phase change Ra #(410 km)	Ra_{410}	4.07×10^8
Phase change Ra #(660 km)	Ra_{660}	7.24×10^8
Gravitational acceleration	g	10 m s^{-2}
Coefficient of thermal expansion	α	3×10^{-5} K^{-1}
Reference density	ρ_0	3500 kg m^{-3}
Slab/upper mantle density contrast	$\Delta\rho$	3.9%
Clapeyron slope, 410 km	γ_{410}	3.0 MPa K^{-1}
Clapeyron slope, 660 km	γ_{660}	−3.5 MPa K^{-1}
Nondimensional γ, 410 km	γ'_{410}	0.0175
Nondimensional γ, 660 km	γ'_{660}	−0.0204
Density change at 410 km	$\Delta\rho_{410}$	4.5%
Density change at 660 km	$\Delta\rho_{660}$	8.0%
Width of the phase transitions	W_{pc}	20 km
Nondimensional T' of PC at 410 km	T_{410}	0.9965
Nondimensional T' of PC at 660 km	T_{660}	0.99879

[a]The Rayleigh number is defined using the Earth's radius as in the work by *Zhong et al.* [2000].

and Helffrich, 1994; *Weidner and Wang*, 1998; *Helffrich and Wood*, 2001]. The strength of the phase change is controlled by:

$$Ra_{pc} = \frac{\Delta\rho_{pc} g R^3}{\kappa\eta_0}, \tag{4}$$

where $\Delta\rho_{pc}$ is the density difference of the phase change. The deflection of the phase change boundary due to temperature, Γ, is given by:

$$p_r = \rho g(1 - r - d_{pc}) - \gamma(T - T_{pc}), \tag{5}$$

$$\Gamma = \frac{1}{2}\left(1 + \tanh\left(\frac{p_r}{\rho g W_{pc}}\right)\right), \tag{6}$$

where p_r is the reduced pressure, r is the radial direction, γ is the Clapeyron slope of the phase change, T is the temperature, and d_{pc} the depth, W_{pc} the width, and T_{pc} the temperature at which the phase change occurs. The phase change temperature, depth, and Clapeyron slopes are nondimensionalized as:

$$T' = \frac{T}{\Delta T}, \tag{7}$$

$$d'_{pc} = \frac{d_{pc}}{R}, \tag{8}$$

and

$$\gamma' = \gamma\left(\frac{\Delta T}{\rho_0 g R}\right). \tag{9}$$

[19] Horizontal numerical resolution was typically ~25 km with a mesh of 129 elements in the vertical, with ~17 km spacing from the surface to 660 km, ~18 km spacing from 660 to 1200 km, ~20 km spacing from 1200 to 1800 km, and ~36 km spacing from 1800 km to the core mantle boundary (CMB). Resolution tests (Appendix D) show that our computations converge under successive refinement and that global misfit differences of 0.2° are within the error of the upper mantle element spacing for the moderate resolution computations employed for convenience. The regions which show the greatest relative variation, though minor, in absolute misfit values are those with sparse gCMT coverage within a depth bin. Higher resolution would lead to insignificant increases in accuracy with a significant increase in computational resources.

[20] To incorporate density anomalies in a mantle circulation model, we convert the regionalized upper mantle (RUM) model of *Gudmundsson and Sambridge* [1998] into temperature. RUM slabs are contours of seismicity based on the *Engdahl et al.* [1998] earthquake catalog. RUM contours are converted to 100 km wide polygons and interpolated at 50 km depth intervals. Our goal is to quantify slab viscosity to first order, so a 3.9% density anomaly, corresponding to a 1300 K temperature anomaly, is prescribed for most models and remains constant throughout the slab. For some models, we prescribed a 1.8% density anomaly, corresponding to a 600 K temperature anomaly, to explore end-member estimations of the expected thermal anomaly for subducting slabs. The lithosphere extends from the surface to 100 km for most models and was modeled as a fluid with viscosity η_0, $10\eta_0$, $100\eta_0$, and $1000\eta_0$, where η_0 is the upper mantle reference. For selected models, we reduced the lithosphere and slab thickness to 50 km, maintaining the same 3.9% density anomaly, further exploring younger slabs. Lithospheric age will control the thermal structure of slabs, but we vary the buoyancy and thickness separately because effective thickness might depend on rheological factors other than temperature. Below the lithosphere, we control the slab viscosity (η_{slab}) with a temperature-dependent rheology $\eta = \eta_0 \exp(E(\Delta T))$. Here, E determines the strength of the temperature dependence and ΔT is the temperature difference between

the slab and the ambient mantle. Since our nondimensional slab temperature is zero and the upper mantle temperature is unity, the maximum slab viscosity is $\eta_0 \exp(E)$. Values for E were chosen to most closely match the lithosphere viscosity which is controlled by a preexponent factor (1–1000) applied to the lithospheric layer.

[21] The asthenosphere is applied globally as part of the radial viscosity structure, extending from the base of the lithosphere to 300 km. The asthenosphere was modeled with viscosities (η_{asth}) of η_0, $0.1\eta_0$ and $0.01\eta_0$. In models with a reduced viscosity asthenosphere, the temperature dependence of the RUM slabs was increased in the asthenospheric layer inversely proportional to the viscosity reduction in the surrounding asthenosphere to maintain the same slab viscosity throughout the upper mantle. We also explored limiting the asthenosphere to beneath oceanic regions only, by excluding continental areas defined by 3SMAC [*Nataf and Ricard*, 1996] when applying the reduction in viscosity to the asthenospheric layer. Results were similar to models with a globally applied asthenosphere and we have excluded these from the discussion.

[22] The lower mantle extends from 660 km to 2891 km and was modeled with viscosities (η_{LM}) of η_0, $10\eta_0$, $30\eta_0$, and $100\eta_0$. Models with no viscosity increase in the lower mantle produced consistently poor matches to gCMTs and we have excluded these results from the discussion.

[23] Surface boundary conditions are either free slip (FS models) or prescribed NUVEL-1A [*DeMets et al.*, 1990] plate motions, either in the no net rotation reference frame of *DeMets et al.* [1990] (NNR models), or the HS3 absolute plate motion model of *Gripp and Gordon* [2002] (HS3 models). For NNR and FS models, we use a free slip boundary condition at the core mantle boundary (CMB). For HS3 models, we use a no-slip CMB boundary condition to induce net rotation related shearing [e.g., *Conrad and Behn*, 2010]. Fixing the CMB and prescribing absolute plate motion models with net rotation, channels the net rotation flow into the upper mantle, roughly consistent with the dynamically induced net rotations from geodynamic models [*Zhong*, 2001; *Becker*, 2006]. Our stiff slab models also induce net rotations self-consistently, as discussed below.

[24] Phase transitions in the upper mantle enhance or reduce the effect of buoyancy forces within cold slabs [e.g., *Turcotte and Schubert*, 2002]. The olivine-spinel phase change at 410 km aids subduction due to the upward deflection of the phase change within the cold slab, increasing negative buoyancy and promoting increased extension at intermediate depths. The postspinel to perovskite + magnesiowüstite phase change at 660 km produces a downward deflection of the phase boundary in the slab, decreasing negative buoyancy. Penetration of the slab into the lower mantle can be hindered by the magnitude of the negative Clapeyron slope of the 660 km phase change [e.g., *Christensen and Yuen*, 1984; *Christensen*, 1996; *Kirby et al.*, 1996] or promote ponding at the lower mantle [*Steinbach et al.*, 1993; *Christensen*, 1996]. We explore the role of phase changes by testing several NNR and HS3 models with and without phase changes, using end-member parameters given in Table 1.

[25] While upper mantle slabs are defined by seismicity and tomography as narrow features descending from oceanic lithosphere in active subduction zones, tomographic images of slabs in the lower mantle are more diffuse and of ambiguous extent. Thus, the influence of lower mantle slabs on flow and deformation is difficult to determine. Lower mantle density anomalies are here inferred from seismic tomography [e.g., *Hager and Clayton*, 1989]. For selected models, we combine upper mantle RUM slabs with lower mantle density anomalies inferred from the mean S wave model (SMEAN) of *Becker and Boschi* [2002]. In these models, the RUM slabs are used for buoyancy and rheology in the first 700 km and the SMEAN tomography is used for buoyancy only in the lower mantle. Motivated by previous, similar studies (e.g., review by *Forte* [2007]), we scale velocity anomalies to density as $dlnV_s/dln\rho = 0.25$.

3.2. Results

[26] We now provide an overview of all models discussed here, explore similarities between the best performing models in terms of global and regional misfit variations, show how they are affected by our global parameter choices, and discuss what this implies for the radial and lateral viscosity structure of the Earth. We then discuss the effect of phase changes, lower mantle density contributions, boundary conditions, net rotation, and regional variations.

3.2.1. Global Model Performance

[27] We evaluated 517 flow models in total and present in Table 2 the global angular eigenvector misfit averages for 216 selected models. The global misfits presented in Table 2 represent the average of the misfits from the 30 subduction zone segments

Table 2. Misfit for 216 Models[a]

× η_0		NNR Global Misfit (deg)								HS3 Global Misfit (deg)							FS Global Misfit (deg)			
			Asth = $0.1\eta_0$					Asth = $0.01\eta_0$			Asth = $0.1\eta_0$				Asth = $0.01\eta_0$			Asth = $0.1\eta_0$		
Slab η	LM η	$\eta_{asth} = \eta_0$: N	N	TH	RA	PC	RS	N	PC	$\eta_{asth} = \eta_0$: N	N	TH	RA	PC	N	PC	$\eta_{asth} = \eta_0$: N	N	TH	Asth = $0.01\eta_0$: N
1	10	39	38	38	38	39	39	38	39	38	37	37	37	38	38	38	39	39	38	39
1	30	39	38	38	38	39	38	39	39	37	37	37	37	38	39	39	39	39	38	39
1	100	39	38	38	38	39	38	39	39	37	37	37	37	38	39	39	39	39	38	39
10	10	40	39	37	38	40	38	38	39	38	37	37	35	39	38	39	40	39	38	39
10	30	39	39	37	39	40	38	38	39	36	36	36	35	38	38	38	40	39	38	39
10	100	39	39	37	39	40	39	39	39	36	36	36	36	38	38	38	39	39	38	39
100	10	47	43	38	45	44	49	42	44	43	41	37	40	42	42	43	47	44	38	41
100	30	43	42	37	42	43	43	42	43	37	37	36	37	39	38	39	45	42	38	40
100	100	42	41	37	41	43	42	42	42	37	37	36	36	38	38	40	44	41	38	41
1000	10	58	56	46	53	52	61	55	50	58	60	45	56	55	58	54	58	52	41	47
1000	30	52	51	45	50	50	54	49	48	50	49	44	49	49	50	49	50	47	40	44
1000	100	49	47	45	47	47	47	47	47	43	44	39	45	43	44	44	48	45	39	44

[a]HS3, NUVEL-1A, HS3 reference frame surface velocities with no-slip CMB; NNR, NUVEL-1A, NNR reference frame with free slip CMB; FS, surface free slip with free slip CMB; N, radial viscosity and upper mantle buoyancy and viscosity only, with no additional effects; TH, 50 km thick slab; RA, Rayleigh number modified for a 1.8% density anomaly corresponding to a temperature anomaly of 600° K (Rayleigh = 1.629×10^8); PC, N models plus phase transitions at 410 km and 660 km; RS, N models plus SMEAN tomography in the lower mantle. Except for TH models, slab and lithosphere thickness is 100 km.

evaluated. In Figure 3 we show the regional misfit for the globally best performing HS3 model for slabs with a 3.9% density anomaly. Models consistently perform near random in areas of extreme arc curvature, where extension persists to ~500 km. These regions are best matched with strong slabs, but the difficulty of generating significant compression at the lower mantle to match gCMTs results in high misfit.

[28] Several general trends are reflected in Table 2. Best performing models, when evaluated based on global misfit, are dominated by those with upper mantle slab viscosities of 10–100η_0 and at least a 1 order of magnitude reduced viscosity asthenosphere. Deviations from solely buoyancy-driven deformation occur from bending and unbending of the slab, and the compressional effect of the lower mantle viscosity. As slab strength increases, bending deformation dominates and slab geometry controls deformation. While slab geometry remains constant between models, lower mantle viscosity exerts a secondary control on deformation. The propagation of compression upward within the slab is controlled by the strength of the lower mantle and of the slab. Weak slabs (1–10η_0) are more easily deformed by the lower mantle viscosity increase and perform slightly better with a 30η_0 lower mantle viscosity. As slab strength increases, comparable, and often stronger, lower mantle viscosities are preferred. Phase transitions act to enhance the same deformation patterns obtained from models without phase

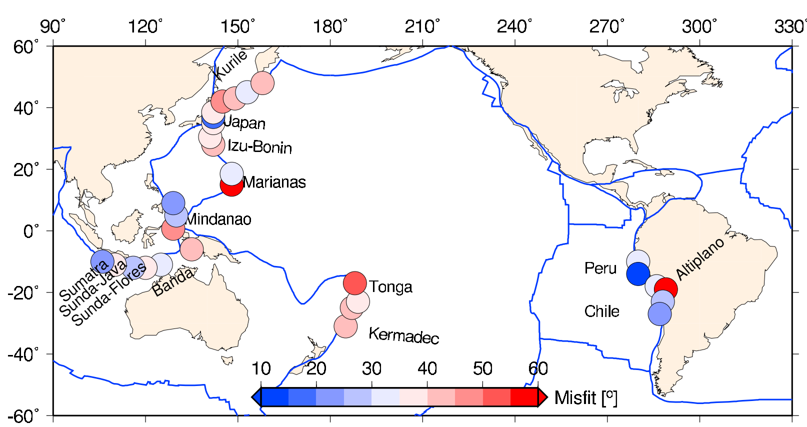

Figure 3. Regional misfit for a single, globally best performing HS3 model with a 3.9% density anomaly and 100 km thick slab and lithosphere. Slab viscosity is 10η_0, with no viscosity reduction in the asthenosphere, and a 100η_0 lower mantle viscosity. The average misfit for the model is 36.0° with a minimum of 14.2° and a maximum of 57.6°.

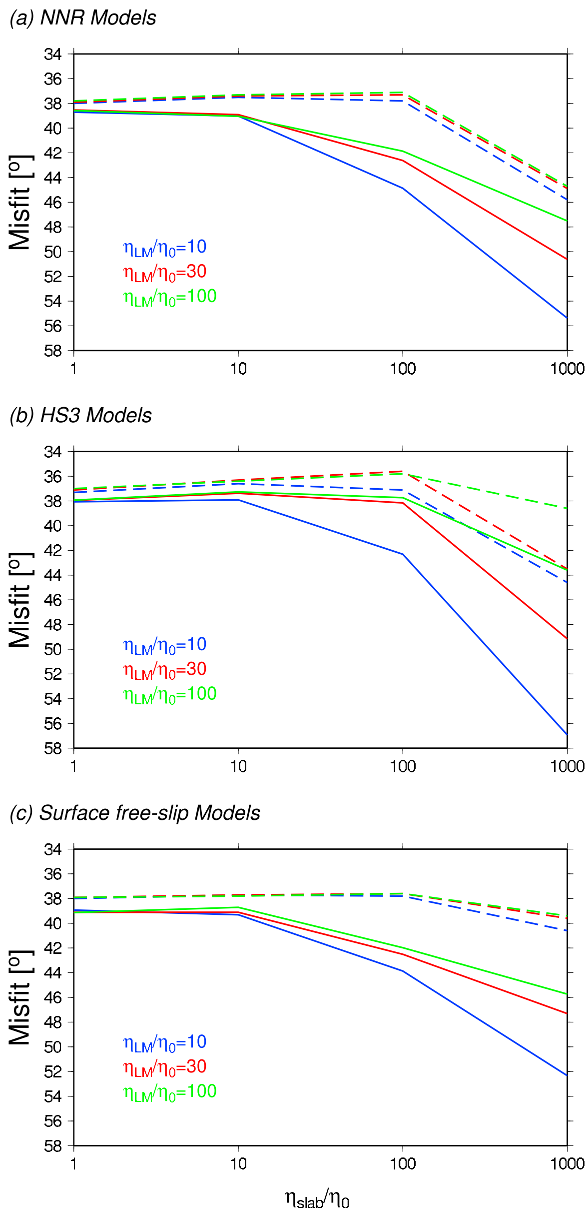

Figure 4. Average model misfits as a function of η_{slab}/η_0 for various lower mantle viscosities for (a) NNR, (b) HS3, and (c) surface free slip models. Each colored line represents a different value of η_{LM}/η_0 used in the global model. Solid lines are for all N models (100 km thick, 3.9% density anomaly) listed in Table 2. Dashed lines are models with a 50 km thick lithosphere and slab (TH models of Table 2).

changes, so their effect is obscured until slab viscosities reach $1000\eta_0$. For these slabs, the dominant extensive deformation is not overcome by lower mantle viscosity increases below $100\eta_0$, so the additional compression from the 660 km phase change improves the match. Lower mantle density anomalies produce insignificant changes in global misfit, but improve misfits for regions with dominant compression.

[29] Surface free slip models perform similar to prescribed velocity models, though our results highlight the importance of net rotations for global flow models. HS3 models, with a no-slip CMB, perform better than NNR and surface free slip models as a whole (Table 2, HS3 models), substantiating the suggestion by *Carminati and Petricca* [2010] that the net rotation of the lithosphere can induce compression in west directed slabs and extension in east directed slabs.

[30] We follow with an evaluation of the global results in terms of each of the modeling parameters, and then discuss regional variations, describing regions that illustrate our interpretations. The latter are, however, based on numerical evaluation of all subduction zones analyzed here.

3.2.2. Slab Strength

[31] Global model performance as a function of slab viscosity is presented in Figure 4 for each boundary condition. Thin, cool slabs (50 km thick and average ΔT of 1300°) and thick, warm slabs (100 km thick, average ΔT of 600°), perform similar to thick, cool slabs (average ΔT of 1300°) in terms of global misfit. However, well-performing thin (TH models of Table 2) and warm (RA models of Table 2) slab models have slab strengths up to $100\eta_0$ whereas thick slabs often show increased misfit values at these strengths (Table 2). From our flow models, we observe that in the absence of kinematic forces, slabs are predominantly extensive at intermediate depths and compressive at the lower mantle. The stronger the slab, the deeper the extensive signal and the stronger the lower mantle must be to generate compression. Best performing surface free slip models have slab viscosities less than $100\eta_0$. For kinematic models, additional force imposed by the surface velocity propagates into the slab (representing incompletely modeled global plate driving forces). These models perform best for slab viscosities of $100\eta_0$ if lower mantle viscosities are comparable.

[32] Regional variations (Figure 3) partially reflect the variable slab geometries seen in Figure 2. As expected from theory and modeling such as *Houseman and Gubbins* [1997], we find that compression dominates in areas of unbending and extension in areas of bending. With increasing viscosity, the compressive unbending signal strengthens

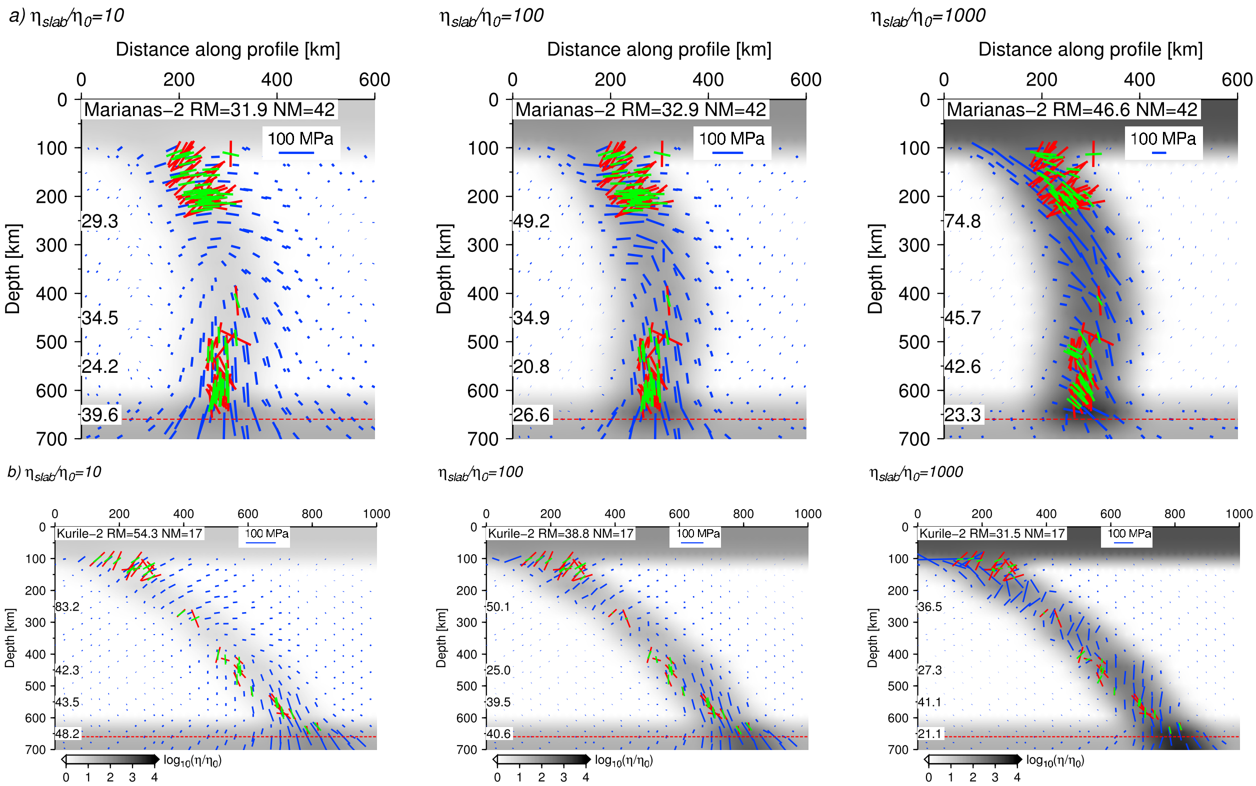

Figure 5. Effect on stress orientations of increasing η_{slab}/η_0 for (a) Marianas and (b) Kurile slabs for an NNR model with $\eta_{LM} = 30\eta_0$ and $\eta_{asth} = \eta_0$. Blue lines show the P axes of stress from flow models. Line lengths are scaled to the second stress tensor invariant and normalized by the maximum magnitude within the slab (below 200 km) for plotting purposes (see label inset). Red lines show the P axes from gCMT solutions, and green lines show the P axes of the interpolated flow stress that was compared to the gCMT. Compressional axes misfit values (in degrees) for each depth range containing gCMT solutions are listed on the left at the corresponding midbin depth. RM, regional misfit (average of depth bin misfits); NM, number of gCMTs used for comparison. The dashed red line indicates the 660 km viscosity jump. Background shading is viscosity.

and, in some cases, propagates throughout the slab (Kurile slab (Figure 5b)). Extension dominates for strongly concave slabs like the Marianas, but with increasing viscosity compression propagates from unbending regions of the slab toward bending regions, resulting in regions of compression on the less concave surface, and extension beneath (Marianas (Figure 5a)).

[33] Thin slabs (TH models of Table 2) are more easily compressed, producing a better match to gCMTs for regions with intermediate compression not matched by thicker, strong slabs. Warmer slab models (RA models of Table 2) perform similar to comparable cooler slab models (N models of Table 2), suggesting that slab deformation is more sensitive to slab thickness than to density variations. For surface free slip models, our conclusions are independent of density contrast as only the stress amplitudes change and not the orientations.

3.2.3. Asthenospheric Strength

[34] Global misfit values improve for most models with the addition of an asthenospheric layer of reduced viscosity below the lithosphere (Table 2). Therefore, we explored parameter ranges in more detail for these models. Strong slabs are more sensitive to the asthenosphere viscosity and show improvement with increasing asthenosphere viscosity reduction (Figure 6). With increasing lower mantle viscosity, the differences are minimized and the models become less sensitive to asthenospheric viscosity, except for HS3 models, where the match degrades with the addition of an asthenosphere for lower mantle viscosities greater than $10\eta_0$ (Figure 6). This results from channeling the net rotation component into the asthenosphere, discussed below.

[35] Regionally, a low-viscosity asthenosphere reduces intermediate depth extension and allows

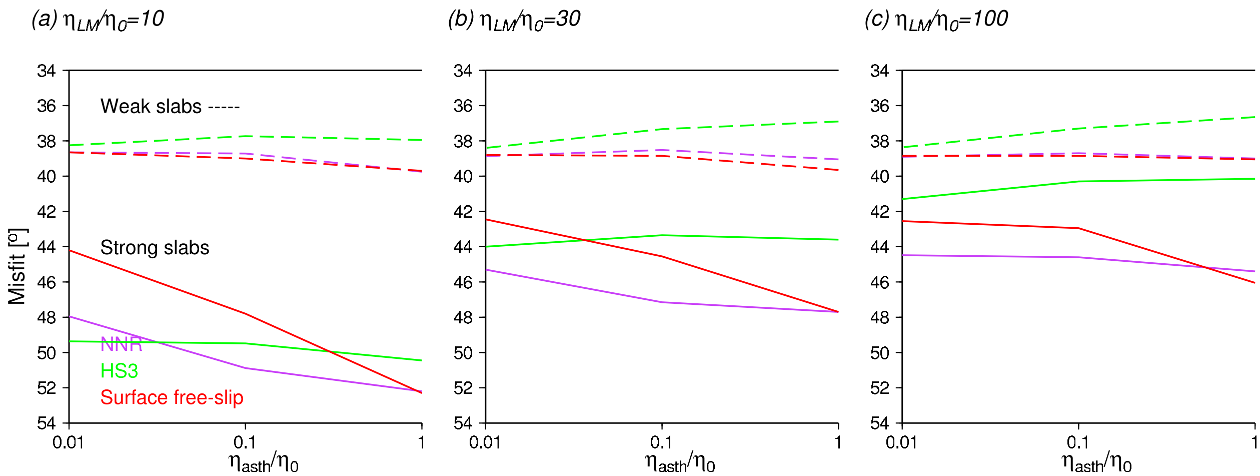

Figure 6. Global misfit as a function of asthenosphere viscosity for strong slabs ($\eta_{slab}/\eta_0 \geq 100$, solid lines) and weak slabs ($\eta_{slab}/\eta_0 \leq 10$, dashed lines) for lower mantle viscosities of (a) $10\eta_0$, (b) $30\eta_0$, and (c) $100\eta_0$. Each colored line represents a boundary condition: NNR plate motions, HS3 plate motions with a fixed CMB, or surface free slip. All models included have a 100 km thick slab and lithosphere and a 3.9% density anomaly.

compression from the lower mantle to propagate upward through the slab. For regions with intermediate depth compression, the match to gCMTs is improved. The effect is significant for $1000\eta_0$ slab viscosities (Table 2) where extension is otherwise dominant.

3.2.4. Lower Mantle Strength

[36] Global model performance as a function of lower mantle viscosity is presented in Figure 7. Results show that lower mantle viscosities of ~30–$100\eta_0$ produce the best match to gCMTs. Increasing the lower mantle beyond $30\eta_0$ has a negligible effect for most models, except for very strong slabs. Testing lower mantle viscosities of $200\eta_0$ produced the same global misfit as models with a $100\eta_0$, with insignificant regional differences. This is in agreement with *Vassiliou and Hager* [1988] who found that increasing the lower mantle viscosity beyond $50\eta_0$ did not significantly change resulting stress magnitudes. As seen in Table 2, the best performing models in terms of global misfit are those in which the slab and lower mantle viscosity contrasts are less than 1 order of magnitude.

[37] Regionally, for all slabs in our fluid models, an increase in viscosity in the lower mantle will promote compression at the slab tip that propagates upward through the slab with increasing lower mantle viscosity, improving the match to gCMTs for regions with dominant compression. Our resurvey of gCMTs indicates that all deeply extending slabs undergo predominantly compressional deformation upon interaction with the lower mantle (Figure 2). Weak slabs and thin slabs are more easily compressed and are therefore less sensitive to increasing lower mantle viscosity (Figure 7). Strong slabs (100–$1000\eta_0$) require a greater increase in lower mantle viscosity to become compressed in the absence of unbending (Figure 8).

3.2.5. Phase Transitions

[38] Global misfits for models with phase transitions included (PC models of Table 2) are improved with the addition of a phase change only for slab viscosities of $1000\eta_0$. The addition of the 410 km and 660 km phase changes generate intermediate extension and deep compression, which are patterns readily attained in flow models without phase transitions. Strong slabs require high lower mantle viscosities to become compressed so the compression generated by the 660 km phase change is noticeable in the global misfit results.

[39] Regionally, for weak slabs, the 410 km phase change improves intermediate depth misfit while the 660 km phase change is less significant because the lower mantle viscosity increase generates enough compression to produce a good match to gCMTs. For strong slabs whose geometry induces intermediate compression contrary to observations, the 410 km phase change improves the misfit at intermediate depths. Accordingly, regions with observed intermediate depth compression show poorer matches with the addition of the phase changes due to the extension generated by the 410 km transition.

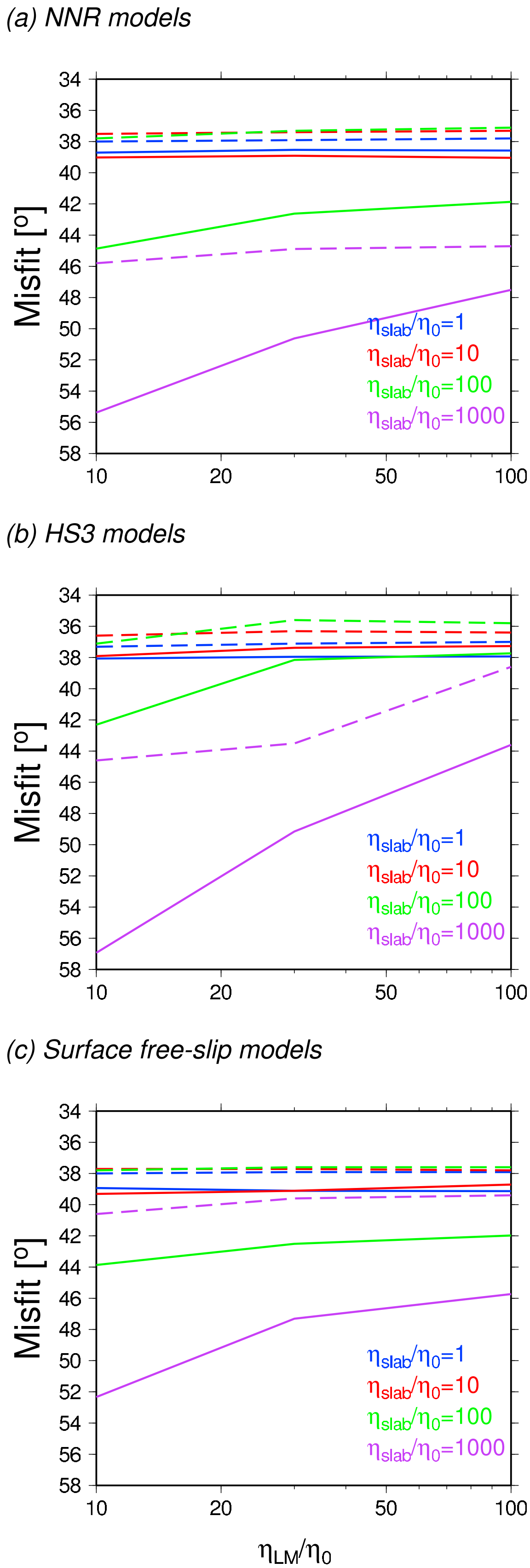

Figure 7. Average model misfits as a function of η_{LM}/η_0 for various slab viscosities for (a) NNR, (b) HS3, and (c) surface free slip models. Each colored line represents a different value of η_{slab}/η_0 used in the global model. Solid lines are for all N models (100 km thick, 3.9% density anomaly) listed in Table 2. Dashed lines are models with a 50 km thick lithosphere and slab (TH models of Table 2).

For stronger lower mantle viscosities, the effect of the 410 km phase change is overwhelmed by the compression induced by the lower mantle viscosity.

3.2.6. Lower Mantle Density Anomalies

[40] Globally, including lower mantle density anomalies produced insignificant changes in the match to gCMTs for weak slabs (Table 2). For strong slabs and weak lower mantle viscosity, global model results worsened with the inclusion of lower mantle density anomalies. Regionally, in areas with lower mantle downwellings inferred from SMEAN, the pull from the lower mantle increased extension throughout the slab. For strong slabs and weak lower mantle viscosity, the increased extension could not be overcome and the slab remains in extension at depth, producing poorer matches to gCMTs. With increasing lower mantle viscosity, values are improved as compression increases at the slab tip. In regions of lower mantle upwelling inferred from SMEAN, increased compression from the lower mantle improves the match to gCMTs for dominantly compressive regions such as Tonga. This supports the work of *Gurnis et al.* [2000] who infer from tomography that the Tonga region overlies the edge of the Pacific superplume and attribute the significant compressional deformation in the Tonga slab to the rising plume.

3.2.7. Surface Boundary Conditions and Net Rotations

[41] Global misfit values from Table 2 show that surface free slip models perform similar to NNR and HS3 for most models. For slab viscosities of $1000\eta_0$, free slip models perform the best. NNR and surface free slip models improve with the addition of a reduced viscosity asthenosphere. HS3 model results are similar to, or improve with a $0.1\eta_0$ asthenospheric viscosity reduction, but results are worse for a higher-viscosity reduction.

[42] Regionally, differences result from the ability of the model to affect intermediate depth deformation

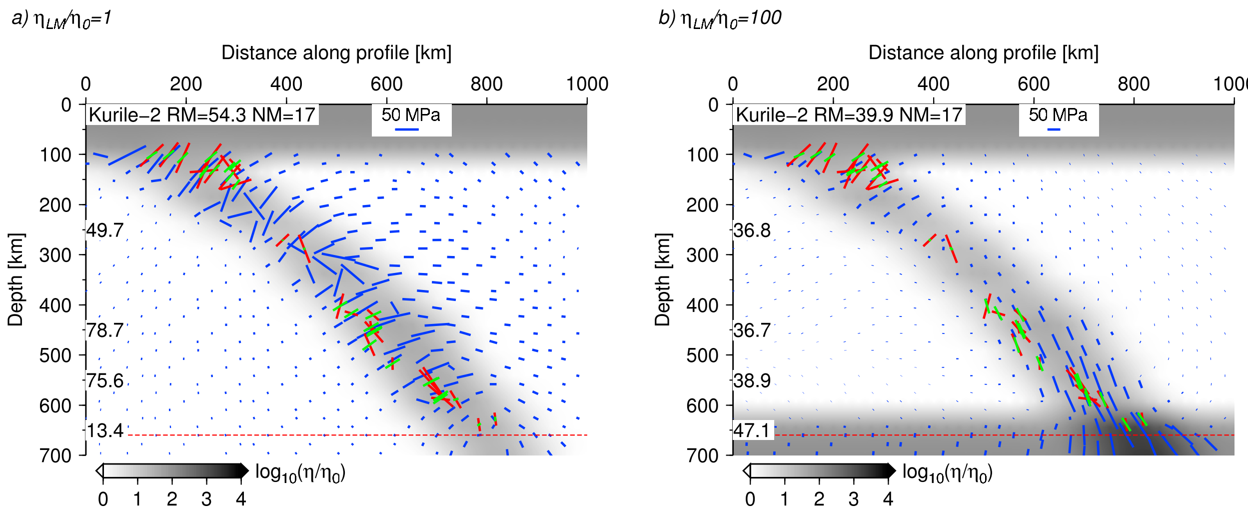

Figure 8. Effect on stress orientations of increasing the lower mantle viscosity from (a) $\eta_{LM} = 1$ to (b) $\eta_{LM} = 100$ for an NNR model with $\eta_{slab}/\eta_0 = 100$ and $\eta_{asth} = \eta_0$. Predominantly compressive regions such as the Kuriles show improved matches to gCMTs with stronger lower mantle viscosities.

patterns and to better reflect the asymmetry observed in Figure 1. Surface free slip models generate intermediate extension, NNR models generate some intermediate depth compression, and HS3 models generate strong intermediate depth compression for west directed regions and extension for east directed regions. The two factors controlling this pattern are the propagation of additional force from the kinematic surface boundary, and the amount of induced net rotation of the lithosphere with respect to the lower mantle.

[43] Surface free slip models generally produce intermediate depth extension that increases with increasing lithospheric strength, and compression at the lower mantle that propagates upward with increasing lower mantle strength. Strong, free slip slabs are difficult to compress and therefore perform poorly compared to NNR or HS3 models that generate intermediate depth compression. However, strong, free slip slabs induce a net rotation of the lithosphere with respect to the lower mantle with an Euler pole similar to that of HS3. The amount of induced net rotation peaks for slab viscosities of $100\eta_0$ (Figure 9) and increases deep compression. Without prescribed surface kinematics, however, these models fail to generate significant intermediate compression, producing minor changes in global misfit values until slab viscosities reach $1000\eta_0$. At these viscosities, the net rotation generates compression in these otherwise dominantly extensive slabs, improving misfit values for most regions and improving global misfits (Table 2).

[44] Misfit values for surface free slip models with weak zones are intermediate between NNR and surface free slip models without weak zones. Weak zones were used only for comparing net rotations generated in surface free slip models and were implemented by reducing the lithospheric viscosity 2 orders of magnitude 100 km to both sides of the NUVEL-1A [*DeMets et al.*, 1990] plate boundaries,

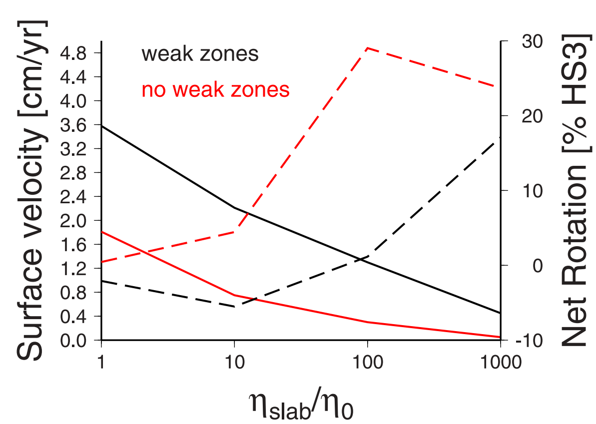

Figure 9. Mean surface velocity versus slab viscosity for surface free slip and surface free slip with weak zone models with a $\eta_{LM}/\eta_0 = 30$ and a $\eta_{asth}/\eta_0 = 0.1$. Right axis (dashed lines) shows net rotation in percent of HS3 computed by $(\underline{\omega}_{HS3} \cdot \underline{\omega}_{model}/|\underline{\omega}_{HS3}|^2)$, where $\underline{\omega}$ is the Euler pole of the net rotation (mean mantle no-net-rotation (MM-NNR) reference frame [cf. *Zhong*, 2001]). Slabs with unity viscosity compared to the upper mantle produce a slight net rotation due to LVVs produced by the reduced viscosity asthenosphere. Negative values for the net rotation as a percent of HS3 are produced by a net rotation opposite in sense to that of HS3.

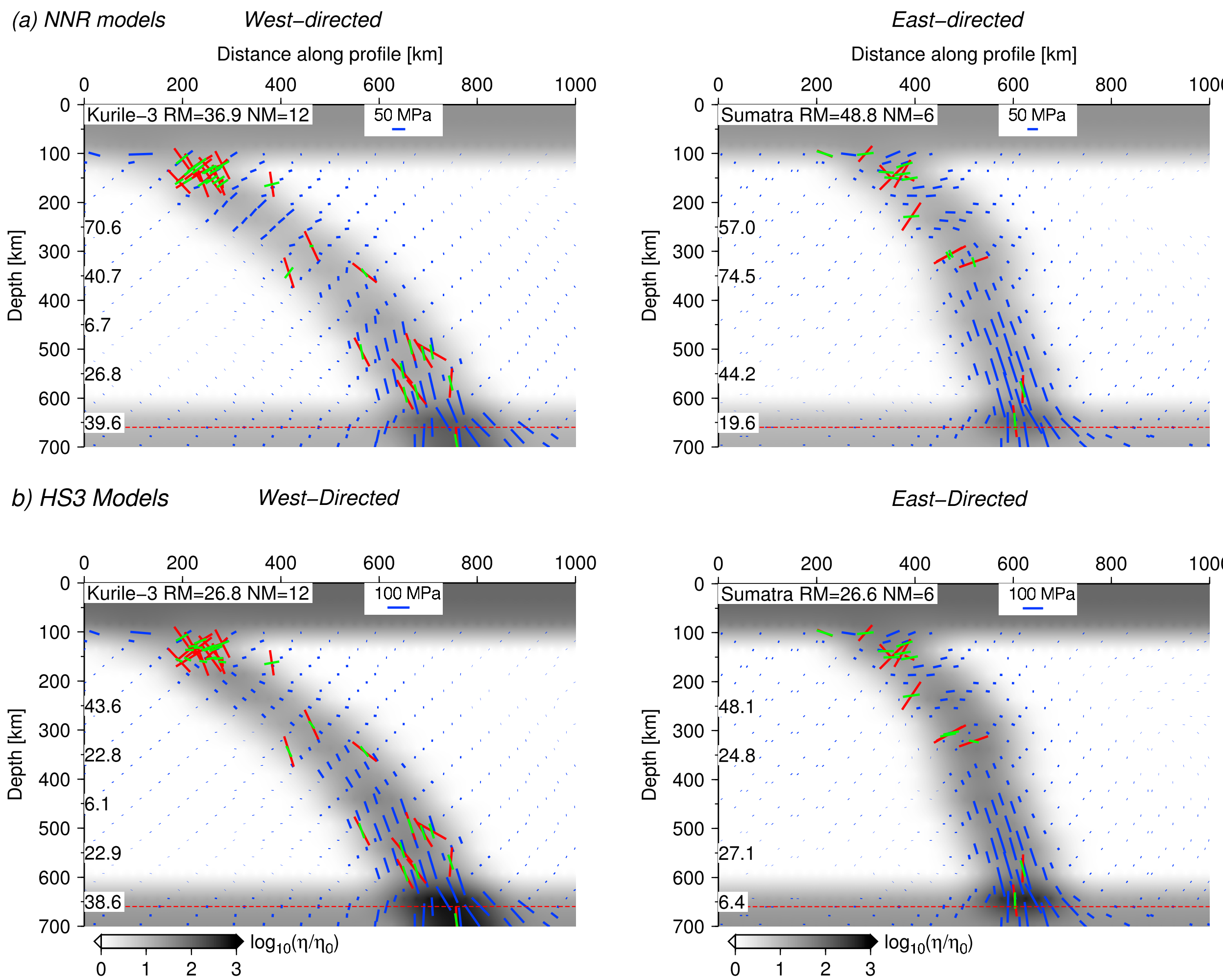

Figure 10. Comparison of stress orientations between (a) NNR and (b) HS3 models on (left) the northwest directed Kurile-3 slab and (right) the east directed Sumatra slab. Slab viscosity is $100\eta_0$, and lower mantle viscosity is $30\eta_0$. The induced net rotations in the HS3 models generate increased compression at intermediate depths for west directed slabs and increased extension for east directed slabs.

from the surface to the base of the lithosphere. Weak zones produce more plate-like motion of the surface, but reduce the strength of the net rotations generated by LVVs (Figure 9). The amount of net rotation induced by stiff, upper mantle slabs is comparable to that induced by stiff continental keels [*Becker*, 2006] and significantly larger that the net rotations based on global, lower-resolution slab models [*Zhong*, 2001; *Becker and Faccenna*, 2009].

[45] The high net rotation HS3 models with a fixed CMB generate greater amounts of compression for west directed slabs, and the induced upper mantle shear generates extension in east directed slabs (Figure 10), reducing the compressive signal generated by the imposed surface velocity. HS3 models then perform better than NNR for regions that are predominantly compressive (Figure 11), but they cannot generate enough extension in east directed slabs to perform better than surface free slip models in dominantly extensive regions. HS3 models without an asthenosphere perform as well as models with a 0.1 reduced viscosity asthenosphere. However, if the asthenosphere is weakened beyond $0.1\eta_0$, the net rotation is channeled into the asthenosphere instead of smoothly decreasing through the upper mantle, reducing the effect of the induced shear below 300 km. As HS3 is thought to invoke too large a net rotation component based on global anisotropy modeling [*Becker*, 2008; *Kreemer*, 2009; *Conrad and Behn*, 2010], we explored various net rotation magnitudes for a suite of models. While the changes are minor, matches to gCMTs scale with increasing net rotation (Figure 12). Global misfit results for these models are provided in Appendix E. The finding that net rotations break the symmetry of coseismic strain patterns and improve the global

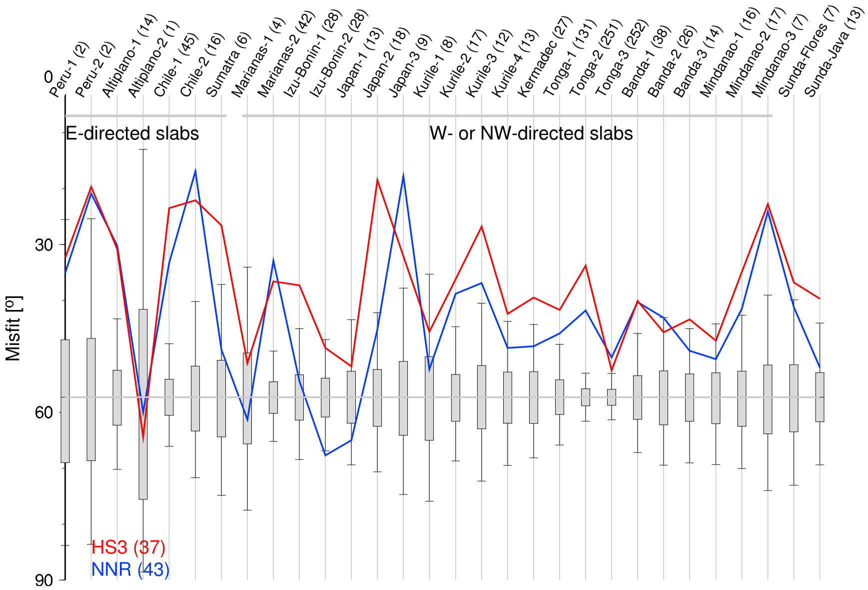

Figure 11. Effect on regional and global misfit values of induced net rotations with prescribed plate motions and a fixed CMB (HS3 models) compared to NNR models, for a model with $\eta_{slab}/\eta_0 = 100$, $\eta_{LM}/\eta_0 = 30$, and $\eta_{asth} = \eta_0$. Misfit values increase downward (models improve upward). Subduction zones are ordered approximately clockwise around the Pacific but are adjusted to have subduction polarity grouped by east directed and west directed. The number of gCMTs used to calculate each misfit value is indicated in parentheses following each region name. Also for each region, box-and-whisker plots show the distribution of misfits for an equivalent number of randomly oriented compression axes in terms of the 50% and 95% confidence bounds, computed by simulation. The average misfit for a random distribution is 57.3°, shown by a horizontal gray line. Global misfits are indicated in parentheses in the bottom left corner.

misfit substantiates the work by *Carminati and Petricca* [2010], although the mechanics of force transmission are different in our global models.

[46] However, as shown next, regional variations in slab strength may reduce the gCMT misfit of both NNR and HS3 to similar levels, without having to invoke net rotations.

3.2.8. Regional Model Performance

[47] Figure 13 shows the selection of global models that lead to the best regional misfit for HS3 boundary conditions, which shows the spatial variability of our best fit models. By mixing flow models this way, the misfit can be reduced significantly (from 36° to 28.8°), though the proper test would be, of course, to allow for regional variations in a single global model, which we do not attempt here.

[48] Figure 14 shows that best fitting slab viscosities are depth dependent. Here, we compare NNR and HS3 best fitting slab strengths by region for three depth ranges. From 200 to 350 km, most regions are best matched with slab viscosities of 100–1000η_0; from 350 to 500 km, most regions are best matched by slab viscosities of 10–100η_0; and from 500 to 700 km, most regions are best matched by slab viscosities of 100η_0. Average misfit values for each boundary condition and depth range (Figure 14) indicate that HS3 models perform slightly better in terms of regional misfit than NNR models at the 350–500 km depth range. This depth range represents the transition from dominantly extension to dominantly compression for most regions. From 500 to 700 km, HS3 models dominate the best fit

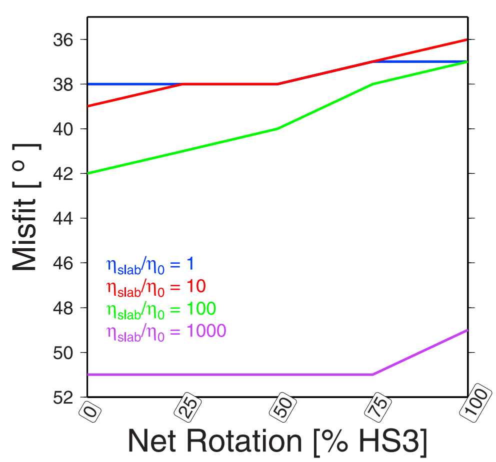

Figure 12. Effect on misfit values of increasing net rotation component for variable slab viscosities for a model with $\eta_{asth}/\eta_0 = 0.1$ and $\eta_{LM}/\eta_0 = 30$.

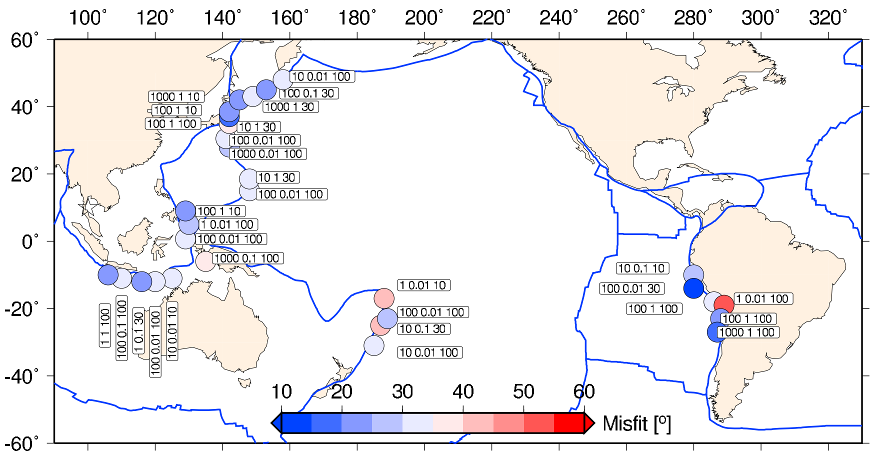

Figure 13. Best fit viscosity model for each region for all HS3 boundary condition models with thick slabs and a 3.9% density contrast and only radial and lateral viscosity variations (i.e., no phase changes or lower mantle density). The average misfit for the model is 28.8° with a minimum of 10.8° and a maximum of 50.5°. Results for NNR models produce similar patterns. The first number is the η_{slab}/η_0, the second is the η_{asth}/η_0, and the third is the η_{LM}/η_0.

results, however, the average regional misfit values are similar to those of the NNR models.

4. Discussion

[49] Our best performing global models have a misfit of ~36°, as expressed by the global misfit measure (Table 2). The best models always perform much better than expected from randomness (Figure 11), and this is also the case for almost all regional subduction zone profiles for slab viscosities below $1000\eta_0$. Moreover, there are robust trends of misfit values with parameters such as lower/upper mantle viscosity contrast. This gives us confidence that our interpretation as to the dynamic role of these parameters in a fluid modeling context are robust and useful, and that the global circulation model can be used as a backdrop against which to improve a dynamic description of subduction zone stress. The viscosity increase in the lower mantle that is preferred by our models is consistent with estimates obtained from geoid modeling [e.g., *Hager and Clayton*, 1989; *Forte*, 2007], and the relatively low effective slab strength (10–100 times the upper mantle) supports "weak slab" models (see, e.g., review by *Becker and Faccenna* [2009]).

[50] While it is difficult to make such statements with statistical rigor, the remaining misfit of our best models appears too large to be explained by uncertainties in the gCMT parameters or modeling inaccuracies (Figure 3). Although we are somewhat limited by the resolution of our input models and the representation of plate boundaries, based on our assessment of numerical stability (Appendix D), we consider it more likely that the physical assumptions are incomplete. There are a range of effects that were not considered, including elasto-plastic rheologies, the effect of the crust, phase transitions in minerals other than olivine, compositional heterogeneity, and the preexistence of planes of weakness in the slab. Incorporation of some of these effects (lithospheric age, crustal thickness and sediment load) are better suited to regional studies. Other effects relate to more complicated rheology (e.g., effects of elasticity and mechanical anisotropy) which could be incorporated into future models. Effects of elasticity could clearly be important, and would introduce stress memory into the system.

[51] Besides elasticity we feel that two effects are perhaps most important when trying to refine our models further, that of regional variation and that of existing planes of weakness (e.g., faults). Figure 13 shows that regionally, misfit can be improved by using different parameters, and one may expect that locally varying effects such as lithospheric age, crustal thickness, or sediment load will play an important role, for example in affecting regional slab viscosity. While such effects could be included in our models [cf. *Wu et al.*, 2008], we decided not to optimize our global model in such a way, so as to not complicate the model too far.

[52] Zones of weakness may, for example, be due to volatile assisted faulting [e.g., *Ranero et al.*, 2003; *Faccenda et al.*, 2008] and existing structures may still play a role in controlling faulting at depth [e.g., *Jiao et al.*, 2000; *Warren et al.*, 2008]. If mechanical anisotropy in subducted lithosphere matters below depths of 200 km, our simplified association of

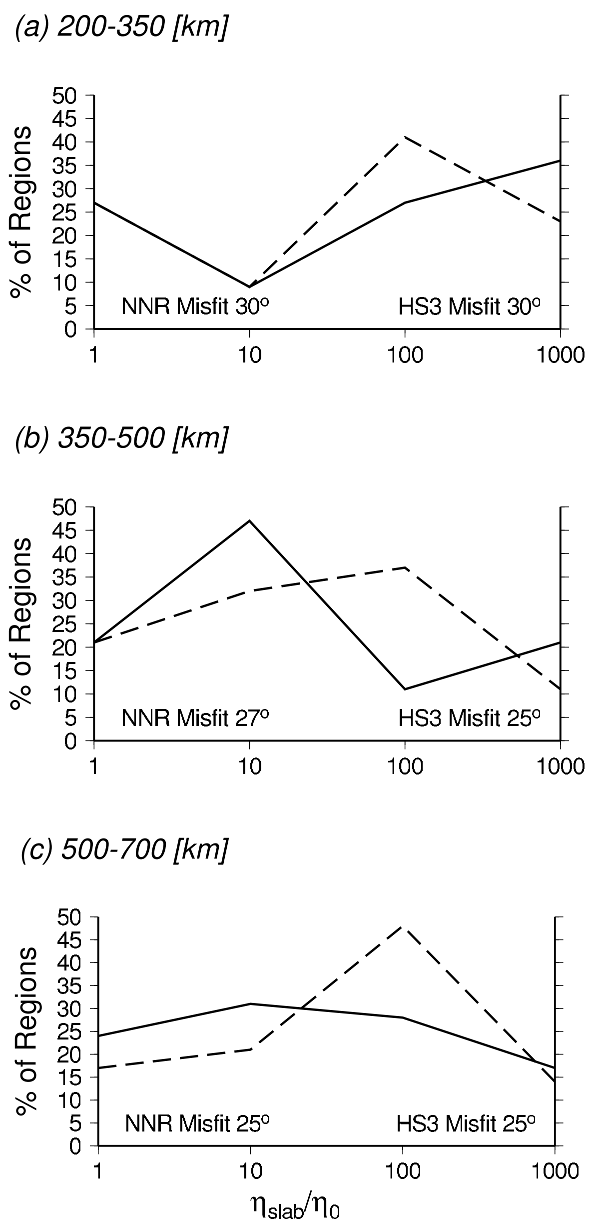

Figure 14. Best fitting slab strengths for NNR models (solid lines) and HS3 models (dashed lines) for depth ranges of (a) 200–350 km, (b) 350–500 km, and (c) 500–700 km. For each region, we find the global model that produces the lowest misfit value. We plot the percent of regions whose best fit model has the same slab viscosity as a function of $\eta slab$. The average global misfit for the depth range and boundary condition is indicated.

seismic strain release and stress will break down, and such effects may well explain the remaining misfit at intermediate depths. Incorporating mechanical anisotropy into a deterministic model would require detailed assumptions about subducted structure and material behavior, but could in principle be attempted, assisted by regional modeling [e.g., *Faccenna et al.*, 2009].

[53] The true evaluation of the relative importance of the effects which are ignored here has to wait until we have models that are able to incorporate a more complete rheological description of slabs. However, the results here indicate that our initial mechanical treatment is suitable to explain the first-order features of subduction zone deformation consistently over a global scale.

5. Conclusions

[54] The global deformation patterns of subducting slabs show that strain release complexity is ubiquitous at intermediate depths. Broadly, regions can be separated into predominantly intermediate extension for east directed subduction zones and intermediate compression for west directed subduction zones. Best performing models suggest that slabs may not be stronger than ~10–100 times the upper mantle viscosity to match the observed deformation pattern if the fluid model provides a valid baseline.

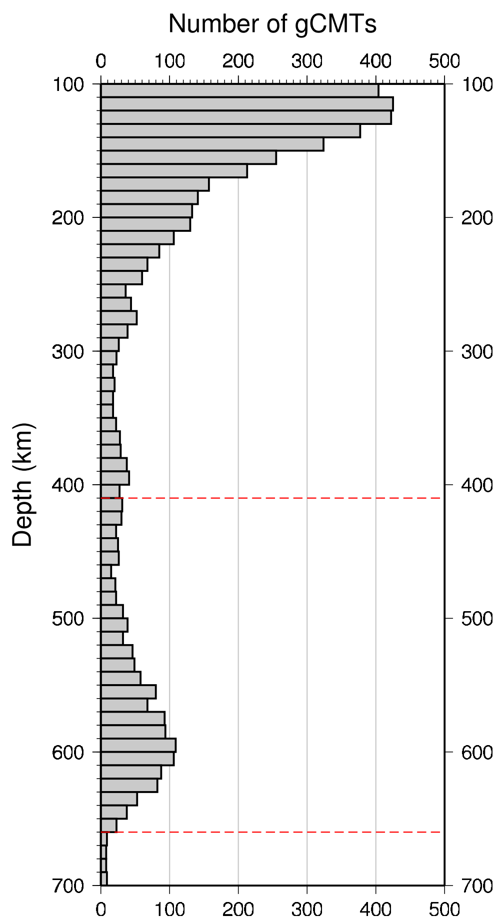

Figure A1. Global distribution of gCMTs with depth. Dashed red lines mark 410 km and 660 km phase transitions.

Table B1. Subduction Zone Parameters Used to Construct Profiles

Region Name	Longitude (deg)	Latitude (deg)	Azimuth (°CW From N.[a])	Width (km)	Length (km)
Marianas	140	17	90	200	1000
Tonga North	180	−18.2	65	75	900
Tonga South	179	−20	120	150	900
Japan	129	42	100	450	1700
Kurile	147	52	140	650	1200
Izu-Bonin North	134	31	60	150	900
Izu-Bonin Central	137	25.9	50	150	900
Izu-Bonin South	138	23	50	150	900
Kermadec	176	−30	115	250	800
Calabrian	11.5	41.5	120	100	600
Peru	290	−6	250	500	1200
Chile	300	−24	270	500	1400
New Hebrides North	173	−11.5	250	400	800
New Hebrides South	173	−17.3	250	150	500
Sunda Flores	118	−3	180	300	1200
Sunda Java	112	−2	200	300	1200
Mindanao North	120	9	90	300	1000
Mindanao South	121	4	110	300	1000
New Zealand	172	−34	135	250	1000
New Britain	149	−2.5	140	250	600
Solomons	158	−4	220	200	800
Middle America	273	19	215	500	900
Aleutians	184	58	160	400	1000
Banda	124.1	−5.9	82	50	1200
Ryukyus	124	30	140	400	800
Sumatra	106	2	240	500	1200
South Sandwich	326	−58	90	300	700
Hindu Kush	74	34	330	200	800
Luzon	126	20	270	100	1000

[a]Degrees clockwise from north.

Regionally, one control on deformation is slab geometry, as viscous bending produces compression in areas of unbending and extension in areas of bending. Increasing slab strength increases the importance of viscous bending in controlling deformation. Most models improve with the addition of a reduced viscosity asthenosphere and our results support at least a 1 order of magnitude reduction in viscosity. Slab strength may be spatially variable as well as depth dependent.

[55] To obtain compression at the slab tip while maintaining some intermediate depth extension, lower mantle viscosities must be ~30–100 times the upper mantle viscosity, as suggested by *Vassiliou and Hager* [1988]. In addition to radial and lateral viscosity variations, the inclusion of phase changes at 410 km and 660 km produce increased intermediate depth extension and deep compression. Phase changes affect the global misfit only for strong slabs and weak lower mantle models, where compression at the slab tip is otherwise negligible. Lower mantle density anomalies also increase extension in areas of downwellings, and increase compression in upwelling regions, such as underneath Tonga [cf. *Gurnis et al.*, 2000].

[56] Our best performing global models are those that have net rotations of the surface with respect to the lower mantle larger than those typically excited by the slabs themselves [cf. *Carminati and Petricca*, 2010]. These models generate compression in west directed slabs and the induced shear produces extension in east directed slabs, a symmetry breaking effect that may alternatively be explained by regional variations in no net rotation models.

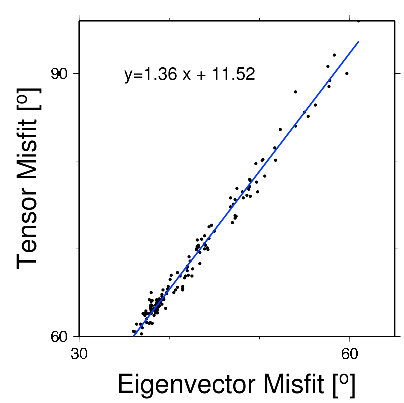

Figure C1. Eigenvector versus tensor misfit for all thick (100 km), 3.9% density anomaly, slab models reported in Table 2.

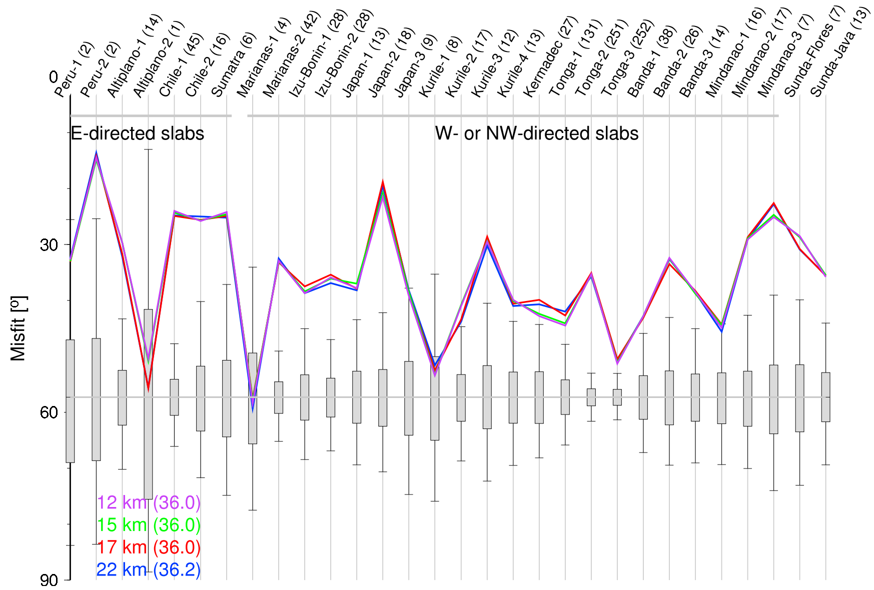

Figure D1. Misfit by region as a function of upper mantle resolution. Upper mantle element spacing and global misfit in degrees is listed in parentheses in the bottom left corner.

[57] These results point to the need for further study of combined high-resolution slab and keel models including realistic plate margins and proper match to relative and absolute plate velocities. Our study shows that global circulation models explain first-order features in slab seismicity and so provide useful constraints on upper mantle dynamics.

Appendix A: Earthquake Distribution With Depth

[58] We define intermediate depth as 100 km to 350 km and deep as 350 km to 700 km, based on the global distribution of gCMT solutions with depth. Figure A1 shows the centroid depth distribution for the gCMT catalog (Global CMT Project, 2006, available at http://www.globalcmt.org/, accessed May 2008) from 1976 to 2008. The seismicity minima at ~350 km corresponds as well to the transition depth at which predominately extensional deformation becomes predominately compressional deformation, as noted by *Isacks and Molnar* [1971].

Appendix B: Subduction Zone Parameters

[59] In Table B1 we provide the parameters used to construct our cross sections for the purpose of identifying the slab deformation state shown in Figure 2. Parameters were chosen to most closely replicate the cross sections of *Isacks and Molnar* [1971] but were occasionally adjusted when structural complexities required a distinct profile to investigate differences along strike.

Appendix C: Correlation Between 3-D Vector and Tensor

[60] Figure C1 shows the correlation between the P axes, eigenvector misfits, as used to characterize model performance, and the more complete tensor inner product misfit. The eigenvector misfit is calculated as arccos($|\mathbf{e}_{cmt} \cdot \mathbf{e}_{stress}|$), where $\mathbf{e}_{cmt}$ is the compressional eigenvector of the gCMT solution and $\mathbf{e}_{stress}$ is the compressional eigenvector of the stress solution from the fluid model. The tensor misfit is calculated using the inner product as arccos ($\mathbf{T}_{cmt}$: $\mathbf{T}_{stress}$), where $\mathbf{T}_{cmt}$ is the gCMT and $\mathbf{T}_{stress}$ is full stress tensor solution from the fluid model. Considering the correlation, we report only the more intuitive eigenvector misfits in Table 2 and the main text.

Appendix D: Resolution Tests

[61] In an effort to evaluate the error associated with the numerical resolution, we compare various upper mantle resolution models and find that our computations converge under successive refinement. Global misfit differences of 0.2° are within the error of the upper mantle element spacing (Figure D1).

Table E1. Misfit Results in Degrees as a Function of Increasing Net Rotation Component, From NNR to HS3[a]

$\times\eta_0$		η_{asth}/η_0 = 0.1: Net Rotation Magnitude and Global Misfit (deg)				
Slab η	LM η	NNR	0.25 NR	0.50 NR	0.75 NR	HS3
1	10	38	38	38	38	37
1	30	38	38	38	37	37
1	100	38	38	38	37	37
10	10	39	38	38	37	37
10	30	39	38	38	37	36
10	100	39	38	38	37	36
100	10	43	44	43	43	41
100	30	42	41	40	38	37
100	100	42	41	39	37	37
1000	10	56	58	59	59	60
1000	30	51	51	51	51	49
1000	100	47	46	45	45	44

[a]Models with net rotation have a fixed CMB while NNR models have a free slip CMB. Models have a $0.1\eta_{asth}/\eta_0$ applied globally. We also evaluated an NNR model with a fixed CMB and found that the results matched to within the error of our resolution the results of the same model with a free slip CMB.

CitcomS computations were performed on a multigrid solver with a minimum overall accuracy of 10^{-3} for the divergence in the Uzawa iterations for incompressibility.

[62] For our study, the vertical resolution would most likely have an influence on our phase change models as the phase change transition width (20 km) is similar to our mesh resolution in the transition zone (~18 km). To address this, we performed a model with a 40 km transition width. The global misfit difference between the models (0.15°) is within our overall resolution. Regional differences were insignificant, with a maximum difference of <1.9°, minimum of zero, and average differences of 0.33°.

Appendix E: Global Model Misfit as a Function of Increasing Net Rotation Component

[63] To test the effect of net rotation magnitude on global eigenvector misfit, we tested a suite of models with a globally applied asthenosphere and prescribed surface velocities with variable amounts of net rotation. Our results indicate that the high net rotation absolute plate motions of HS3 produce the best match to gCMTs (Table E1).

Acknowledgments

[64] We thank reviewers Jeroen van Hunen and Magali Billen and Editor James Tyburczy for their helpful comments on an earlier version this manuscript. This material is based upon work supported by the National Science Foundation under grant EAR-0643365. Computations were conducted at the University of Southern California Center for High Performance Computing and Communications (http://www.usc.edu/hpcc). Figures 1–14, A1, C1, and D1 were produced with the GMT software by *Wessel and Smith* [1991].

References

Apperson, K., and C. Frohlich (1987), The relationship between Wadati-Benioff zone geometry and *P*, *T*, and *B* axes of intermediate and deep focus earthquakes, *J. Geophys. Res.*, *92*, 13,821–13,831.
Astiz, L., T. Lay, and H. Kanamori (1988), Large intermediate-depth earthquakes and the subduction process, *Phys. Earth Planet. Inter.*, *53*, 80–166.
Bailey, I., T. Becker, and Y. Ben-Zion (2009), Patterns of co-seismic strain computed from southern California focal mechanisms, *Geophys. J. Int.*, *177*, 1015–1036.
Becker, T. W. (2006), On the effect of temperature and strain-rate dependent viscosity on global mantle flow, net rotation, and plate-driving forces, *Geophys. J. Int.*, *167*, 943–957.
Becker, T. W. (2008), Azimuthal seismic anisotropy constrains net rotation of the lithosphere, *Geophys. Res. Lett.*, *35*, L05303, doi:10.1029/2007GL032928. (Correction, *Geophys. Res. Lett.*, *35*, L08308, doi:10.1029/2008GL033946, 2008.)
Becker, T., and L. Boschi (2002), A comparison of tomographic and geodynamic mantle models, *Geochem. Geophys. Geosyst.*, *3*(1), 1003, doi:10.1029/2001GC000168.
Becker, T., and C. Faccenna (2009), A review of the role of subduction dynamics for regional and global plate motions, in *Subduction Zone Geodynamics*, edited by S. Lallemand and F. Funiciello, pp. 3–34, Springer, Berlin.
Becker, T. W., and R. J. O'Connell (2001), Predicting plate velocities with mantle circulation models, *Geochem. Geophys. Geosyst.*, *2*(12), 1060, doi:10.1029/2001GC000171.
Bevis, M. (1988), Seismic slip and down dip strain rate in Wadati-Benioff zones, *Science*, *240*, 1317–1319.
Bilek, S., C. P. Conrad, and C. Lithgow-Bertelloni (2005), Slab pull, slab weakening and their relation to deep intra-slab seismicity, *Geophys. Res. Lett.*, *32*, L14305, doi:10.1029/2005GL022922.
Billen, M. I. (2008), Modeling the dynamics of subducting slabs, *Annu. Rev. Earth Planet. Sci.*, *36*, 325–356.
Billen, M. I., and M. Gurnis (2003), Comparison of dynamic flow models for the Central Aleutian and Tonga-Kermadec subduction zones, *Geochem. Geophys. Geosyst.*, *4*(4), 1035, doi:10.1029/2001GC000295.
Billen, M. I., M. Gurnis, and M. Simon (2003), Multiscale dynamics of the Tonga-Kermadec subduction zone, *Geophys. J. Int.*, *153*, 359–388.
Bina, C., and G. Helffrich (1994), Phase transition Clapeyron slopes and transition zone seismic discontinuity topography, *J. Geophys. Res.*, *99*, 15,853–15,860.
Carminati, E., and P. Petricca (2010), State of stress in slabs as a function of large-scale plate kinematics, *Geochem. Geophys. Geosyst.*, *11*, Q04006, doi:10.1029/2009GC003003.
Chen, P.-F., C. Bina, and E. Okal (2004), A global survey of stress orientations in subducting slabs as revealed by intermediate-depth earthquakes, *Geophys. J. Int.*, *159*, 721–733.
Christensen, U. R. (1996), The influence of trench migration on slab penetration into the lower mantle, *Earth Planet. Sci. Lett.*, *140*, 27–39.

Christensen, U. R., and D. A. Yuen (1984), The interaction of a subducting lithospheric slab with a chemical or phase boundary, *J. Geophys. Res.*, *89*, 4389–4402.

Conrad, C. P., and M. D. Behn (2010), Constraints on lithosphere net rotation and asthenospheric viscosity from global mantle flow models and seismic anisotropy, *Geochem. Geophys. Geosyst.*, *11*, Q05W05, doi:10.1029/2009GC002970.

Conrad, C. P., and C. Lithgow-Bertelloni (2002), How mantle slabs drive plate tectonics, *Science*, *298*, 207–209.

DeMets, C., R. Gordon, D. Argus, and S. Stein (1990), Current plate motions, *Geophys. J. Int.*, *101*, 425–478.

Deparis, V., H. Legros, and Y. Ricard (1995), Mass anomalies due to subducted slabs and simulations of plate motion since 200 My, *Phys. Earth Planet. Inter.*, *89*, 271–280.

Dziewoński, A. M., T.-A. Chou, and J. H. Woodhouse (1981), Determination of earthquake source parameters from waveform data for studies of global and regional seismicity, *J. Geophys. Res.*, *86*, 2825–2852.

Engdahl, E. R., R. D. van der Hilst, and R. Buland (1998), Global teleseismic earthquake relocation with improved travel times and procedures for depth determination, *Bull. Seismol. Soc. Am.*, *88*, 722–743.

Faccenda, M., L. Burlini, T. Gerya, and D. Mainprice (2008), Fault-induced seismic anisotropy by hydration in subducting oceanic plates, *Nature*, *455*, 1097–1101.

Faccenna, C., E. Di Giuseppe, F. Funiciello, S. Lallemand, and J. van Hunen (2009), Control of seafloor aging on the migration of the Izu-Bonin-Mariana trench, *Earth Planet. Sci. Lett.*, *288*, 386–398.

Fischer, K., and T. Jordan (1991), Seismic strain rate and deep slab deformation in Tonga, *Geophys. Res. Lett.*, *26*, 2121–2124.

Forsyth, D. W., and S. Uyeda (1975), On the relative importance of the driving forces of plate motion, *Geophys. J. R. Astron. Soc.*, *43*, 163–200.

Forte, A. (2007), Constraints on seismic models from other disciplines—Implications for mantle dynamics and composition, in *Treatise on Geophysics*, vol. 1, *Seismology and the Structure of the Earth*, edited by B. Romanowicz and A. Dziewonski, pp. 805–858, Elsevier, Amsterdam.

Fukao, Y., S. Widiyantoro, and M. Obayashi (2001), Stagnant slabs in the upper and lower mantle transition region, *Rev. Geophys.*, *39*, 291–323.

Giardini, D., and J. H. Woodhouse (1984), Deep seismicity and modes of deformation in Tonga subduction zone, *Nature*, *307*, 505–509.

Gripp, A. E., and R. G. Gordon (2002), Young tracks of hotspots and current plate velocities, *Geophys. J. Int.*, *150*, 321–361.

Gudmundsson, O., and M. Sambridge (1998), A regionalized upper mantle (RUM) seismic model, *J. Geophys. Res.*, *103*, 7121–7136.

Gurnis, M., J. Ritsema, H.-J. van Heijst, and S. Zhong (2000), Tonga slab deformation: The influence of a lower mantle upwelling on a slab in a young subduction zone, *Geophys. Res. Lett.*, *27*, 2373–2376.

Hager, B. H. (1984), Subducted slabs and the geoid: Constraints on mantle rheology and flow, *J. Geophys. Res.*, *89*, 6003–6015.

Hager, B. H., and R. W. Clayton (1989), Constraints on the structure of mantle convection using seismic observations, flow models, and the geoid, in *The Fluid Mechanics of Astrophysics and Geophysics*, vol. 4, *Mantle Convection: Plate Tectonics and Global Dynamics*, edited by W. R. Peltier, pp. 657–763, Gordon and Breach Sci., New York.

Hager, B. H., and R. J. O'Connell (1979), Kinematic models of large-scale flow in the Earth's mantle, *J. Geophys. Res.*, *84*, 1031–1048.

Helffrich, G., and B. Wood (2001), The Earth's mantle, *Nature*, *412*, 501–507.

Hirth, G., and D. L. Kohlstedt (2004), Rheology of the upper mantle and the mantle wedge: A view from the experimentalists, in *Inside the Subduction Factory*, *Geophys. Monogr. Ser.*, vol. 138, edited by J. Eiler, pp. 83–105, AGU, Washington, D. C.

Houseman, G. A., and D. Gubbins (1997), Deformation of subducted oceanic lithosphere, *Geophys. J. Int.*, *131*, 535–551.

Isacks, B. L., and P. Molnar (1969), Mantle earthquake mechanisms and the sinking of the lithosphere, *Nature*, *223*, 1121–1124.

Isacks, B., and P. Molnar (1971), Distribution of stresses in the descending lithosphere from a global survey of focal-mechanism solutions of mantle earthquakes, *Rev. Geophys.*, *9*, 103–175.

Jiao, W., P. Silver, Y. Fei, and C. Prewitt (2000), Do intermediate- and deep-focus earthquakes occur on preexisting weak zones? An examination of the Tonga subduction zone, *J. Geophys. Res.*, *105*, 28,125–28,138.

Kirby, S. H., S. Stein, E. A. Okal, and D. C. Rubie (1996), Metastable mantle phase transformations and deep earthquakes in subducting oceanic lithosphere, *Rev. Geophys.*, *34*, 261–306.

Kostrov, B. (1974), Seismic moment release and energy of earthquakes and seismic flow of rock, *Phys. Solid Earth*, *1*, 23–40.

Kreemer, C. (2009), Absolute plate motions constrained by shear wave splitting orientations with implications for hot spot motions and mantle flow, *J. Geophys. Res.*, *114*, B10405, doi:10.1029/2009JB006416.

Lithgow-Bertelloni, C., and M. A. Richards (1995), Cenozoic plate driving forces, *Geophys. Res. Lett.*, *22*, 1317–1320.

Lithgow-Bertelloni, C., and M. A. Richards (1998), The dynamics of Cenozoic and Mesozoic plate motions, *Rev. Geophys.*, *36*, 27–78.

Mitrovica, J. X., and A. M. Forte (2004), A new inference of mantle viscosity based upon joint inversion of convection and glacial isostatic adjustment data, *Earth Planet. Sci. Lett.*, *225*, 177–189.

Moresi, L. N., and M. Gurnis (1996), Constraints on the lateral strength of slabs from three-dimensional dynamic flow models, *Earth Planet. Sci. Lett.*, *138*, 15–28.

Nataf, H.-C., and Y. Ricard (1996), 3SMAC: An a priori tomographic model of the upper mantle based on geophysical modeling, *Phys. Earth Planet. Inter.*, *95*, 101–122.

Ranero, C., J. Phipps Morgan, K. Mcintosh, and C. Reichert (2003), Bending-related faulting and mantle serpentinization at the middle america trench, *Nature*, *425*, 367–373.

Ricard, Y., and C. Vigny (1989), Mantle dynamics with induced plate tectonics, *J. Geophys. Res.*, *94*, 17,543–17,559.

Ricard, Y., C. Doglioni, and R. Sabadini (1991), Differential rotation between lithosphere and mantle: A consequence of lateral mantle viscosity variations, *J. Geophys. Res.*, *96*, 8407–8415.

Stadler, G., M. Gurnis, C. Burstedde, L. Wilcox, L. Alisic, and O. Ghattas (2010), The dynamics of plate tectonics and mantle flow: From local to global scales, *Science*, *329*, 1033–1038, doi:10.1126/science.1191223.

Steinbach, V., D. Yuen, and W. Zhao (1993), Instabilities from phase transitions and the timescales of mantle thermal evolution, *Geophys. Res. Lett.*, *118*, 1119–1122.

Turcotte, D. L., and G. Schubert (2002), *Geodynamics*, 2nd ed., Cambridge Univ. Press, Cambridge, U. K.

van der Hilst, R. D., S. Widiyantoro, and E. R. Engdahl (1997), Evidence for deep mantle circulation from global tomography, *Nature*, *386*, 578–584.

Vassiliou, M. S., and B. H. Hager (1988), Subduction zone earthquakes and stress in slabs, *Pure Appl. Geophys.*, *128*, 547–624.

Vidale, J., and H. Benz (1982), Upper-mantle seismic discontinuities and the thermal structure of subduction zones, *Nature*, *356*, 678–682.

Warren, L. M., M. A. Langstaff, and P. G. Silver (2008), Fault plane orientations of intermediate-depth earthquakes in the Middle America Trench, *J. Geophys. Res.*, *113*, B01304, doi:10.1029/2007JB005028.

Weidner, D., and Y. Wang (1998), Chemical- and Clapeyron-induced buoyancy at the 660 km discontinuity, *J. Geophys. Res.*, *103*, 7431–7441.

Wessel, P., and W. H. F. Smith (1991), Free software helps map and display data, *Eos Trans. AGU*, *72*, 445–446.

Wu, B., C. Conrad, A. Heuret, C. Lithgow-Bertelloni, and S. Lallemand (2008), Reconciling strong slab pull and weak plate bending: The plate motion constraint on the strength of mantle slabs, *Earth Planet. Sci. Lett.*, *272*, 412–421.

Zhong, S. (2001), Role of ocean-continent contrast and continental keels on plate motion, net rotation of lithosphere, and the geoid, *J. Geophys. Res.*, *106*, 703–712.

Zhong, S., M. T. Zuber, L. Moresi, and M. Gurnis (2000), Role of temperature-dependent viscosity and surface plates in spherical shell models of mantle convection, *J. Geophys. Res.*, *105*, 11,063–11,082.